HYBRID RANS/LES SIMULATIONS OF SWIRLING CONFINED TURBULENT JETS

Chris De Langhe, Bart Merci, Koen Lodefier and Erik Dick
Department of Flow, Heat and Combustion Mechanics
Ghent University
Sint-Pietersnieuwstraat 41, B-9000 Ghent, Belgium
Chris.DeLanghe@UGent.be

ABSTRACT

A hybrid RANS/LES model, previously developed by the authors, is validated for turbulent flow in swirling confined jets. The results are compared with the experimental data of Dellenback (1988).

INTRODUCTION

Swirling flows in confined, suddenly expanding, geometries occur in e.g. burners, but also in cyclone dust-separators, dryers and similar devices in chemical process industry. These flow configurations are especially interesting for an approach with hybrid RANS/LES, as it concerns high-Reynolds number flows in confined geometries, which show very complex unsteady behaviour. Especially for high swirl intensities, the unsteadiness of the mean flow is strongly intertwined with that of the turbulent fluctuations, and RANS computations of these flows, even with the most elaborate models, encounter difficulties. Fully wall-resolved LES of these flows is, due to the confined geometries and the high Reynolds numbers, not an option for industrial computations. LES with wall-functions could be tried for burners where the separation point at the expansion is fixed, but will encounter problems when the inlet throat has a rounded shape, and the separation point is no longer geometrically fixed, which is very often the case in burner geometries. In those cases, more accurate modelling of the near-wall region is necessary, and a hybrid RANS/LES method is appropriate.

In this paper we present applications of a hybrid RANS/LES model, recently developed by our group, to swirling flows with a fixed separation point at the expansion. As mentioned, such flows could be adequately modeled using a LES model with wall-functions, and the advantages of using hybrid RANS/LES for these flows are small. Actually, since the near-wall behaviour is of minor importance in these flows, we will use wall-functions with our hybrid RANS/LES model, and therefore this paper should be seen mainly as an investigation of the performance of the LES part of our hybrid model. The RANS activity was restricted to about 1 to 4 near-wall grid cells, the rest of the domain being computed with LES. Computation of more complex exit nozzles, where the application of a hybrid model becomes more interesting, will be considered in future work.

THE MODEL

The previously presented hybrid RANS/LES model (De Langhe, 2003, 2005) functions as a one-equation subgrid model, with a transport equation for the mean dissipation rate $\overline{\varepsilon}$, in LES regions of the flow, and as a two-equation $\overline{K}-\overline{\varepsilon}$ model in RANS regions. In the LES form of the model, the filter width explicitly enters the effective viscosity and the inverse time scale in the $\overline{\varepsilon}$-equation. The transition point from RANS to LES is determined by comparing the filter width to a length scale constructed from the subgrid turbulent kinetic energy and the mean dissipation rate.

In (De Langhe, 2003, 2005) we explained that, for high Reynolds numbers and for the filter width wavenumber Λ_c in the inertial range, the renormalization group (RG) procedure (Giles, 1994a, 1994b) leads to an effective viscosity

$$\nu(\Lambda_c) = a\overline{\varepsilon}^{1/3}\Lambda_c^{-4/3}, \tag{1}$$

with $a = 0.46$, and with the mean dissipation rate $\overline{\varepsilon}$ determined by the transport equation

$$\begin{aligned}\frac{D\overline{\varepsilon}}{Dt} &= \nu(\Lambda_c)\Lambda_c^2\left(C_{\varepsilon 1}P_K - C_{\varepsilon 2}\overline{\varepsilon}\right)\\ &\quad + \frac{\partial}{\partial x_i}(\alpha\nu(\Lambda_c)\frac{\partial\overline{\varepsilon}}{\partial x_i}).\end{aligned} \tag{2}$$

The model constants are

$$\alpha = 1.39 \qquad C_{\varepsilon 1} = \frac{4}{3} \qquad C_{\varepsilon 2} = 2, \tag{3}$$

and $P_K = -\tau_{ij}S_{ij}$ the production of turbulent kinetic energy, with τ_{ij} the Reynolds stress tensor and $S_{ij} = (\partial_j U_i + \partial_i U_j)/2$ the strain rate tensor ($\mathbf{U}$ denotes the resolved velocity field). The subgrid kinetic energy equation used for determining the RANS limit and for post-processing (De Langhe, 2003, 2005) is

$$\frac{D\overline{K}}{Dt} = P_K - \nu(\Lambda_c)\Lambda_c^2\overline{K} + \frac{\partial}{\partial x_i}(\alpha\nu(\Lambda_c)\frac{\partial\overline{K}}{\partial x_i}). \tag{4}$$

The RANS limit follows if $\Lambda_c \leq \Lambda_{es}$, where Λ_{es} is a wave number constructed from the subgrid $\overline{K}$ and $\overline{\varepsilon}$ as

$$\Lambda_{es} = \left(\frac{3}{2}C_K\right)^{3/2}\frac{\overline{\varepsilon}}{\overline{K}^{3/2}} \approx \pi\frac{\overline{\varepsilon}}{\overline{K}^{3/2}}, \tag{5}$$

where C_K is the Kolmogorov constant (calculated by RG (Giles, 1994a) as $C_K = 1.44$). Substitution of Λ_c with Λ_{es} in eqns. (1), (2) and (4) leads to the RANS model

$$\nu = C_\mu\frac{\overline{K}^2}{\overline{\varepsilon}} \tag{6}$$

$$\frac{D\overline{K}}{Dt} = P_K - \overline{\varepsilon} + \frac{\partial}{\partial x_i}(\alpha\nu\frac{\partial\overline{K}}{\partial x_i}) \tag{7}$$

$$\frac{D\overline{\varepsilon}}{Dt} = \frac{\overline{\varepsilon}}{\overline{K}}(C_{\varepsilon 1}P_K - C_{\varepsilon 2}\overline{\varepsilon}) + \frac{\partial}{\partial x_i}(\alpha\nu\frac{\partial\overline{\varepsilon}}{\partial x_i}), \quad (8)$$

with $C_\mu = 0.1$ and the other constants as above.

In practice, the switch between RANS and LES is obtained by taking $\Lambda_c \equiv \pi/L$, where $L = \min\left(\Delta, \frac{\overline{K}^{3/2}}{\overline{\varepsilon}}\right)$ and Δ is the filter width.

For the simulations presented below, the model is extended with a standard wall function formulation. The $\overline{\varepsilon}$-equation is not solved in the first cell, but instead, when P denotes a wall-adjacent cell, the dissipation is computed as

$$\overline{\varepsilon}_P = \frac{C_\mu^{3/4}\overline{K}_P^{3/2}}{\kappa y_P} \quad (9)$$

with $\kappa = 0.39$ the von Kármán constant, $\overline{K}_P$ the turbulent kinetic energy at point P and y_P the distance from point P to the wall. Further, in the wall-adjacent cells, the production term in the turbulent kinetic energy equation is computed as

$$P_K = \frac{\tau_w^2}{\kappa\rho C_\mu^{1/4}\overline{K}_P^{1/2} y_P}. \quad (10)$$

The velocity at the point P is computed from

$$U^* = \frac{1}{\kappa}\ln(Ey^*) \quad (11)$$

where

$$U^* \equiv \frac{\rho U_P C_\mu^{1/4}\overline{K}_P^{1/2}}{\tau_w} \quad (12)$$

and

$$y^* = \frac{C_\mu^{1/4}\overline{K}_P^{1/2} y_P}{\nu_0} \quad (13)$$

with $E = 9.793$ and U_P the mean velocity at point P. When P lies in the RANS zone, these are the standard wall functions, based on equilibrium conditions that are valid in the logarithmic layer. When P lies in the LES zone, the effective viscosity is given by the usual expression (1), with $\overline{\varepsilon}$ computed from (9). In both RANS and LES regimes, $\overline{K}_P$ is computed from the RANS $\overline{K}$-equation with the production term (10). This is a valid assumption, when an equilibrium spectrum (i.e. a constant $\overline{\varepsilon}$ in the inertial range) is assumed in the log-layer.

TEST CASES

For all simulations, the geometry was taken in accordance with the experimental setup (Dellenback, 1988). The expansion ratio is 1 : 2, the length of the inlet pipe is 2 times the inlet diameter D, and the length of the section after the expansion $20D$. In total, 9 experiments for different Reynolds and swirl numbers were performed by Dellenback. In this paper we check the model performance of four of these experiments, namely at $Re = 30 \cdot 10^3$ for $S = 0$, $S = 0.6$ and $S = 0.98$, and at $Re = 100 \cdot 10^3$ for $S = 1.23$. The Reynolds numbers are based on the inlet diameter and the average axial velocity at the inlet (averaged over the cross section). The swirl numbers are also computed at the inlet as the ratio of axial fluxes of swirl and linear momentum (divided by a characteristic radius)(Dellenback, 1988).

The simulations were performed with the commercial CFD-package Fluent, which used a second order central differencing scheme for the momentum equations and second order accurate time discretization. The transport equations for $\overline{K}$ and $\overline{\varepsilon}$ were implemented with the user defined functions in Fluent, and therefore solved using a second order upwind scheme. In all cases, an initial field was obtained from a RANS computation. No initial perturbations were superposed on the velocity field, as the turbulence developed by itself due to the very unstable mixing layer behind the separation point.

The total number of grid points was about $1.8 \cdot 10^5$, the resolution being finest near the expansion, and quite coarse otherwise. As explained before, the flow field is not integrated up to the wall, but wall-functions are used instead, as complex wall effects are supposed to be of minor importance in these flows. The center of the first grid-cell has a near-wall distance $y^+ \approx 30$ in the inlet pipe for the case of $Re = 30 \cdot 10^3$, $S = 0$. With this grid, there is RANS activity in a zone of 1 to 4 near-wall cells. There is also an occasional switch to RANS in some cells in the mixing layer, which is an artifact of comparing the filter width Δ with the subgrid length scale $\overline{K}^{3/2}/\overline{\varepsilon}$ (instead of the integral length scale). As the viscosity varies continuously when switching from LES to RANS, and because they only occur in one or two neighboring cells at a time, these occasional switches to RANS are unlikely to influence the results.

BOUNDARY CONDITIONS

In each test case, the inlet conditions were constructed from a pipe flow simulation, taking into account the specific grid resolution at the inlet. In the available 2D LDA experimental data, only the mean velocity fields and RMS values of the fluctuations are given at the inlet in axial and tangential directions. In order to obtain appropriate inlet conditions, a possible, albeit cumbersome, solution is to perform a separate hybrid RANS/LES simulation of a periodic swirling pipe flow, with grid resolution in all directions equal to that at the inlet of the experimental geometry, and to adjust a tangential body force and Reynolds number such that the mean velocity profiles match the experimental inlet values (Pierce and Moin, 1998). However, inlet profiles for swirling burner geometries are very peculiar, depending on the swirl generator used, and trying to match the mean velocity profile of the periodic simulation with a body force is extremely unpractical. Although it has been experienced that, when only the fluctuations are taken from the periodic simulation (which are then added to the experimental mean velocity profiles), the exact mean velocity profile is not very important (Schlüter et al., 2004), an extra difficulty arises in the case of hybrid RANS/LES, which use one or more transport equations in the subgrid model. Then not only the resolved velocity fluctuations are needed at the inlet, but also values for the solved transport equations in the turbulence model (in the case of our model, the mean dissipation rate and the subgrid turbulent kinetic energy), and these do depend on the correct form of the velocity field. In many cases, values for these quantities are not available from experiments, and if they are, they are the total values and not the subgrid ones. Simple rescalings of these total values to subgrid values often do not work, especially closer to walls.

For the present calculations we use the experimental mean velocity profiles to calculate the production, convection and diffusion term of the subgrid turbulent kinetic energy equation. The destruction term is however made filter-width dependent, in order to scale the subgrid turbulent kinetic energy

according to the filter width. The mean dissipation rate equation is obtained from its RANS transport equation, with the velocity field frozen at the experimental values. The mean subgrid dissipation, mainly happening at the subgrid scales, is well approximated by its RANS value. In this way we obtain, in a very quick and easy manner, mean values for the necessary boundary conditions. Tests for periodic channel flow have shown that this leads to reasonable approximations for the mean subgrid turbulent kinetic energy and dissipation rate. However, in the case of a swirling velocity field, the quality is less satisfying, and could still be improved. Moreover, no fluctuations are generated with this method. The fluctuating content of the velocity could be obtained from a separate LES database, or from some kind of turbulence synthetization. The last option is by far the most practical one, if, of course, a good synthetization algorithm is available.

Because the results for the considered flows were found to be relatively independent from the details of the inlet conditions, we leave the investigation of the inlet conditions and a synthetization algorithm for future work. For the present paper we superpose a simple white noise fluctuation, with a magnitude corresponding to a turbulence level of about 10%, on the inlet velocity field. No fluctuations were imposed on the inlet profiles for $\overline{K}$ and $\overline{\varepsilon}$.

RESULTS

Below we plot the obtained axial and tangential velocity profiles and turbulence intensities for different cross-sections of the considered flows. All quantities are non-dimensionalized with the inlet diameter D and the maximum axial velocity at the inlet U_0.

Figs. 1-3 show the mean axial velocity and turbulence intensities at different streamwise locations, for the case without swirl. The mean velocity profile is well predicted (as could be expected for a simple, non-swirling, expansion). The turbulence intensities have a tendency to be underpredicted just behind the expansion. In these plots, only the resolved part of the turbulence intensities is shown, and the addition of the modelled part will increase the levels somewhat. However, we suspect that not enough fluctuations are generated here when the flow field is convected from the coarse filter width area at the inlet to the higher resolution region near the expansion. For zero swirl number, the flow field is not unstable enough in the inlet pipe, and it is known (Batten et al., 2004, Keating et al., 2004) that, without a turbulence synthetization algorithm, turbulence intensities tend to be underestimated in the first period after grid refinement. As will be seen below, the cases with swirl do not have this problem, as the instability generating mechanism is stronger there, and already occurs in the pipe before the expansion.

Figs. 4-7 show the mean axial velocity and turbulence intensities at different streamwise locations, for the $Re = 30000$ case with swirl intensity $S = 0.6$. As one can see, generally good agreement is obtained.

Figs. 8-11 show the mean axial velocity and turbulence intensities at different streamwise locations, for the case with $Re = 30000$ and swirl intensity $S = 0.98$. General agreement is satisfactory, including the turbulence intensities. This shows that, as the swirl number and thus the unsteadiness upstream of the expansion, is increased, the turbulence intensities can be well predicted without the necessity of a synthetization algorithm. There is some discrepancy in the axial centerline

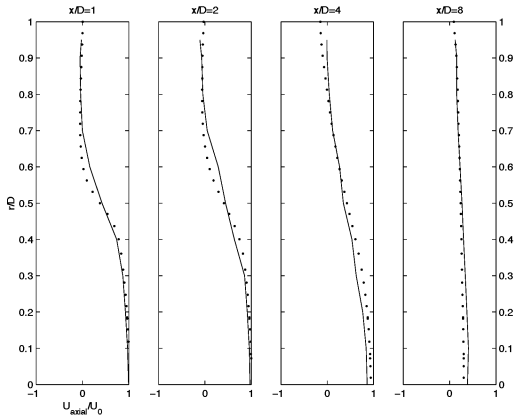

Figure 1: Axial velocity profiles for different positions behind the expansion for $Re = 30000$, $S = 0$. Solid lines: experiment. Dots: hybrid RANS/LES computation.

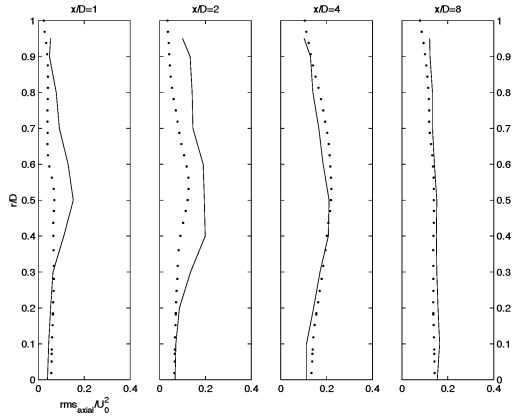

Figure 2: Axial RMS turbulence intensities for different positions behind the expansion for $Re = 30000$, $S = 0$. Symbols as before.

velocity, just behind the expansion, which gives a too large recirculation velocity in our simulation.

Finally, the results for the Reynolds number of 100000 and swirl number of 1.23 (Figs. 12-15), are comparable to those of the previous computation, and we notice a similar overprediction of the recirculation velocity.

CONCLUSION

In general, our simulation results are in good agreement with the experiments for the mean velocity profiles and turbulence intensities. This was accomplished at moderate computational cost, mainly because, for these geometries, wall functions could easily be used, and relatively large streamwise stretching could be applied in the zones further away from the expansion.[1]

Further simulations will be performed to compare these results with unsteady RANS simulations (using full Reynolds stress models) and DES computations of the same geometries.

[1] The largest aspect ratios occur near the wall, where the model is in RANS mode, and thus no significant complications arise with anisotropic filters.

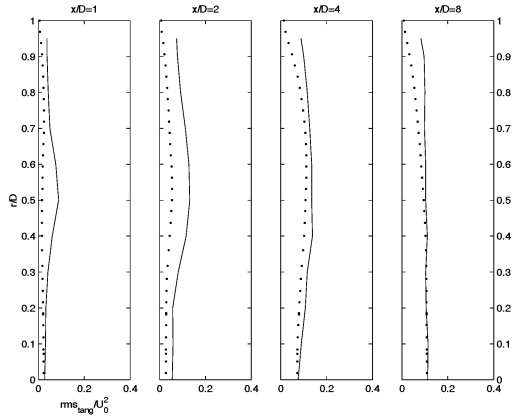

Figure 3: Tangential RMS turbulence intensities for different positions behind the expansion for $Re = 30000$, $S = 0$. Symbols as before.

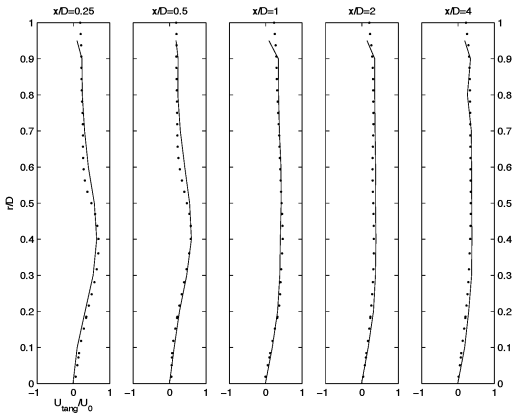

Figure 5: Tangential velocity profiles for different positions behind the expansion for $Re = 30000$, $S = 0.6$. Symbols as before.

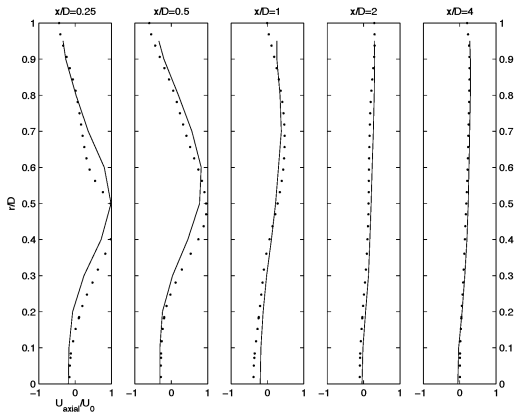

Figure 4: Axial velocity profiles for different positions behind the expansion for $Re = 30000$, $S = 0.6$. Symbols as before.

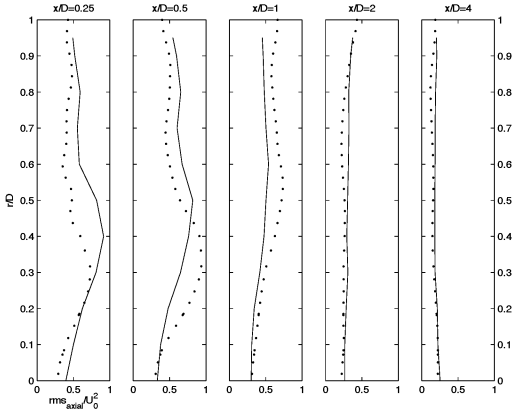

Figure 6: Axial RMS turbulence intensities for different positions behind the expansion for $Re = 30000$, $S = 0.6$. Symbols as before.

It is expected that Reynolds stress models will be able to give reasonable results for moderate swirl numbers (Wegner et al., 2004), but will encounter difficulties at higher swirl numbers, when the precession frequencies become comparable to those of turbulent fluctuations in the low frequency end of the inertial range. Further investigations will also be performed on turbulence synthetization for the inlet conditions and for generating small (i.e. of the size of the filter width) scale turbulence when the flow field is convected from larger to smaller filter width zones. The latter ones can alter the turbulent stresses in the region of the refinement near the expansion, and could lead to further improvements, e.g. in Figs. 2 and 3.

ACKNOWLEDGMENTS

The second author works as a Postdoctoral Fellow for the Fund of Scientific Research - Flanders (Belgium) (FWO-Vlaanderen).

REFERENCES

Batten, P., Goldberg, U. and Chakravarthy, S., 2004, "Interfacing statistical turbulence closures with large-eddy simulation", *AIAA J.*, 42(3):485–492.

De Langhe, C., 2003, "Renormalization Group Approach to Hybrid RANS/LES Modelling", PhD thesis, Ghent University.

De Langhe, C., Merci, B. and Dick, E., 2005, "Hybrid RANS/LES modelling with an approximate renormalization group. I. Model development", Accepted for publication in Journal of Turbulence.

Dellenback, P.A., D.E. Metzger, D.E. and G.P. Neitzel, G.P., 1988, "Measurements in turbulent swirling flow through an abrupt axisymmetric expansion", *AIAA J.*, 26(6):669–681, 1988.

Giles, M.J., 1994a, "Turbulence renormalization group calculations using statistical mechanics methods", *Phys. Fluids*, 6(2):595–604.

Giles, M.J., 1994b, "Statistical mechanics renormalization group calculations for inhomogeneous turbulence", *Phys. Fluids*, 6(11):3750–3764.

Keating, A., Piomelli, U., Balaras, E. and Kaltenbach, H.J., 2004, "A priori and a posteriori tests of inflow conditions for large-eddy simulation", *Phys. Fluids*, 16(12):4696–4712.

Pierce, C.D. and Moin, P., 1998, "Method for generating equilibrium swirling inflow conditions", *AIAA J.*, 36(7):1325–

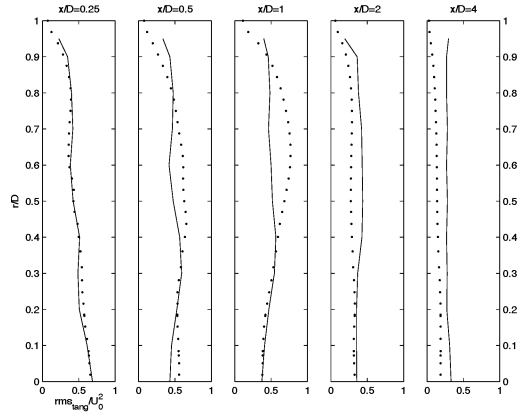

Figure 7: Tangential RMS turbulence intensities for different positions behind the expansion for $Re = 30000$, $S = 0.6$. Symbols as before.

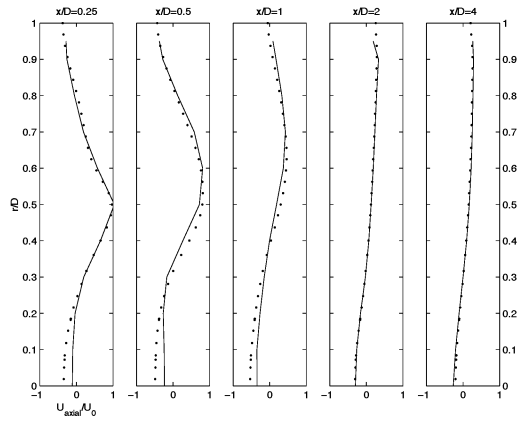

Figure 8: Axial velocity profiles for different positions behind the expansion for $Re = 30000$, $S = 0.98$. Symbols as before.

1327.

Schlüter, J.U., Pitsch, H. and Moin, P., 2004, "Large eddy simulation inflow conditions for coupling with reynolds-averaged flow solvers", *AIAA J.*, 42(3):478–484.

Wegner, B., Maltsev, A., Schneider,C., Sadiki, A., Dreizler, A., and Janicka, J., 2004, "Assessment of unsteady RANS in predicting swirl flow instability based on LES and experiments", *Int. J. Heat and Fluid Flow*, 25:528–536.

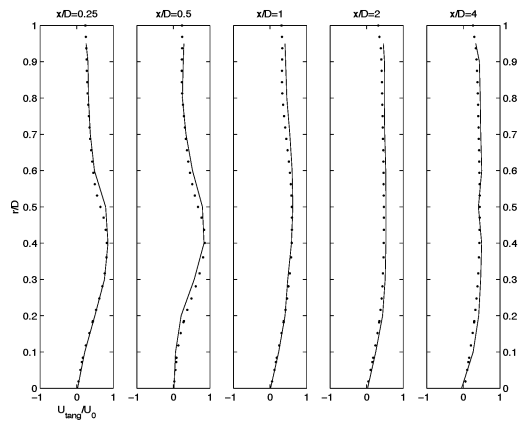

Figure 9: Tangential velocity profiles for different positions behind the expansion for $Re = 30000$, $S = 0.98$. Symbols as before.

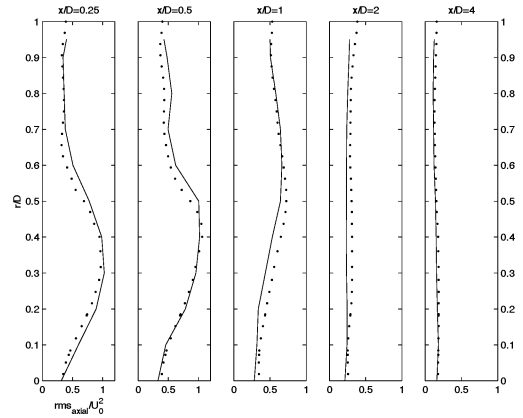

Figure 10: Axial RMS turbulence intensities for different positions behind the expansion for $Re = 30000$, $S = 0.98$. Symbols as before.

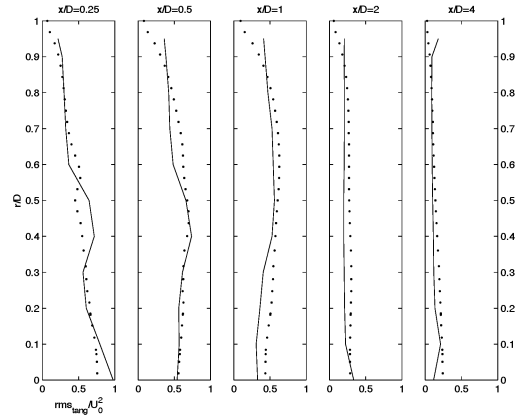

Figure 11: Tangential RMS turbulence intensities for different positions behind the expansion for $Re = 30000$, $S = 0.98$. Symbols as before.

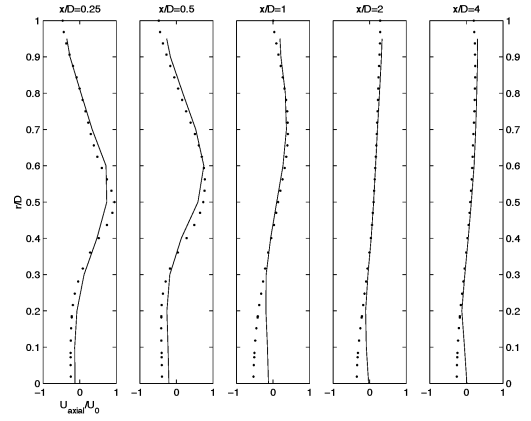

Figure 12: Axial velocity profiles for different positions behind the expansion for $Re = 100000$, $S = 1.23$.

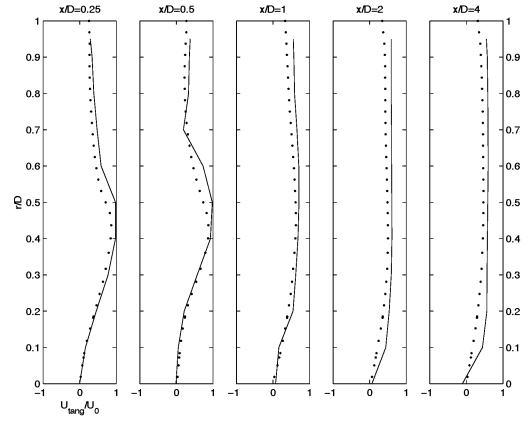

Figure 13: Tangential velocity profiles for different positions behind the expansion for $Re = 100000$, $S = 1.23$. Symbols as before.

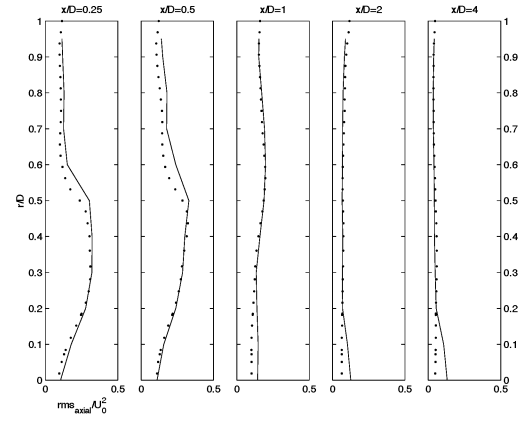

Figure 14: Axial RMS turbulence intensities for different positions behind the expansion for $Re = 100000$, $S = 1.23$. Symbols as before.

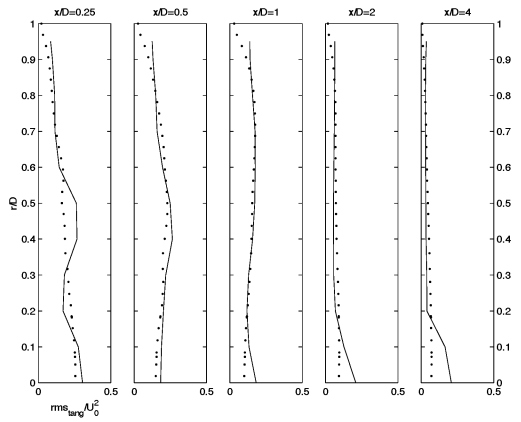

Figure 15: Tangential RMS turbulence intensities for different positions behind the expansion for $Re = 100000$, $S = 1.23$. Symbols as before.